

# **1 The ionospheric gravity and diamagnetic current 2 systems**

P. Alken

3 National Geophysical Data Center, NOAA, Boulder, Colorado, USA

S. Maus

4 National Geophysical Data Center, NOAA, Boulder, Colorado, USA

A. D. Richmond

5 High Altitude Observatory, National Center for Atmospheric Research,

6 Boulder, Colorado, USA

A. Maute

7 High Altitude Observatory, National Center for Atmospheric Research,

8 Boulder, Colorado, USA

---

Patrick Alken, National Geophysical Data Center, NOAA E/GC1, 325 Broadway, Boulder,  
CO 80305-3328, USA. ([patrick.alken@noaa.gov](mailto:patrick.alken@noaa.gov))

9 **Abstract.** Large scale currents in the ionosphere are driven by a vari-  
10 ety of sources, including neutral winds, gravity, and plasma pressure gradi-  
11 ents. While the stronger day-time wind-driven currents have been extensively  
12 studied, gravity and diamagnetic currents in the ionosphere have received  
13 very little attention, but can have substantial effects even during the night.  
14 With the availability of a new generation of magnetic field models based on  
15 high-accuracy satellite magnetic measurements, it becomes increasingly im-  
16 portant to account for these smaller current systems. In this work, we use  
17 the stand-alone NCAR TIEGCM electrodynamics solver along with empiri-  
18 cal density, wind and temperature inputs, to model the global current sys-  
19 tems caused by gravity and diamagnetism in the F-region ionosphere and  
20 calculate their magnetic perturbations. These results allow us for the first  
21 time to visualize the global structure of these currents and quantify their mag-  
22 netic perturbations. We find a significantly higher gravity-driven current dur-  
23 ing the night than one would expect from the lower conductivity which is  
24 primarily due to a Pedersen current driven by polarization charges in the pre-  
25 dawn sector. We find some discrepancies between the diamagnetic pertur-  
26 bation and a theoretical prediction which could be a result of magnetic ten-  
27 sion due to the curvature of the geomagnetic field lines. These results will  
28 allow geomagnetic field modelers to account for these important current sys-  
29 tems and create more accurate models. This work will also be crucial in an-  
30 alyzing ionospheric magnetic field measurements from upcoming satellite mis-  
31 sions such as Swarm.

## 1. Introduction

32 The Earth's ionosphere is divided primarily into two layers, the E-region from about 90  
33 to 150 km altitude, and the F-region from about 150 to 800 km altitude. In the E-region,  
34 currents are mainly driven by neutral winds, resulting in large scale dynamo currents, such  
35 as the equatorial electrojet and the mid-latitude Sq current system. During the night, the  
36 E-region typically disappears due to reduced ionization and its high recombination rate.  
37 In the higher altitude F-region, there are also dynamo currents driven by thermospheric  
38 winds [*Rishbeth, 1971*]. Wind generated electric fields in the F-region are mapped along  
39 field lines to E-region heights. Zonal winds cause vertical current flows at the equator  
40 which divert meridionally into both hemispheres at higher altitudes and then close equa-  
41 torward at lower altitudes. These vertical F-region dynamo currents have been detected  
42 in satellite data [*Maeda et al., 1982; Lühr and Maus, 2006*]. Current systems also exist in  
43 the F-region due to plasma effects. At the equator during daytime, zonal electric fields  
44 created by the global wind dynamo drive vertical ion drift, lifting plasma hundreds of  
45 kilometers upward, until gravity causes it to diffuse down magnetic field lines reaching an  
46 equilibrium roughly 15 degrees on each side of the magnetic equator at F-region altitudes.  
47 This density enhancement is called the Equatorial Ionization Anomaly (EIA).

48 The EIA can enhance two important plasma currents which are of interest in this paper:  
49 the gravity-driven and diamagnetic currents. The gravity-driven current is caused by  
50 plasma interacting with the Earth's gravity and geomagnetic fields, while the diamagnetic  
51 current is driven by plasma pressure gradients. Due to the weak magnetic signature of  
52 both of these current systems (about 10,000 times smaller than the ambient geomagnetic

53 field), it has historically been difficult to identify them in magnetic field measurements.  
54 However, these F-region currents have been found to play an important role in ionospheric  
55 dynamics, particularly during night-time. *Eccles* [2004] studied the F-region gravity-  
56 driven and diamagnetic currents using a coupled ionosphere-electrodynamics model and  
57 found that the gravity-driven current contributes significantly to night-time vertical drift  
58 velocities. *Maus and Lühr* [2006] first identified the gravity-driven current in satellite  
59 magnetic field observations, and found a large latitudinal range of current flowing. *Lühr*  
60 *et al.* [2003] first detected magnetic field depletions in satellite measurements which are  
61 due to the effects of the diamagnetic current. By assuming that the plasma pressure is  
62 exactly balanced by a change in magnetic pressure, they derived a simple formula for the  
63 magnetic field depletion. This assumption is an approximation which neglects changes  
64 in magnetic tension, as we discuss later, and also neglects other forces parallel to the  
65 geomagnetic field, such as gravity and collisions with neutrals, which are important for  
66 balancing parallel pressure gradients. However, this assumption allows an estimation of  
67 diamagnetic corrections which are very important for high-accuracy geomagnetic field  
68 modeling [*Lühr and Maus*, 2010; *Maus et al.*, 2010]. In this paper, we further study these  
69 two important current systems using a modeling procedure based on both first principles  
70 and empirical inputs. Through this work, we are able to study the global flow of the  
71 gravity-driven and diamagnetic currents, as well as study the accuracy of the diamagnetic  
72 effect formula proposed by *Lühr et al.* [2003].

## 2. Ionospheric currents

73 Electric currents in the low and mid-latitude ionosphere are primarily driven by winds,  
74 gravity and plasma pressure gradients. The expression for these currents is given by

$$75 \quad \mathbf{J} = \sigma(\mathbf{E} + \mathbf{U} \times \mathbf{B}) + \mathbf{J}_g + \mathbf{J}_d \quad (1)$$

$$76 \quad \mathbf{J}_g = \frac{nm_i}{B^2} \mathbf{g} \times \mathbf{B} \quad (2)$$

$$77 \quad \mathbf{J}_d = \frac{1}{B^2} \mathbf{B} \times \nabla P \quad (3)$$

78 where  $\sigma$  is the conductivity tensor [Forbes, 1981, eq. 10],  $\mathbf{E}$  is the electric field,  $\mathbf{U}$  is the  
79 neutral wind velocity field,  $n$  is the electron density,  $m_i$  is the ion mass,  $\mathbf{g}$  is the gravita-  
80 tional acceleration,  $\mathbf{B}$  is the ambient geomagnetic field with magnitude  $B$ ,  $P = nk(T_i + T_e)$   
81 is the plasma pressure,  $k$  is the Boltzmann constant,  $T_i$  is the ion temperature, and  $T_e$  is  
82 the electron temperature. The first term on the right hand side of Eq. 1 is responsible  
83 for the main ionospheric currents, including the equatorial electrojet and mid-latitude Sq  
84 currents. These current systems are very prominent in the E-region during the day but  
85 diminish significantly during the night due to a drop in E-region conductivity. The second  
86 term  $\mathbf{J}_g$  represents the gravity-driven current. This term depends on electron density  $n$ ,  
87 and so we would expect this current to be strongest near the equatorial ionization anomaly  
88 (EIA) in the F-region. Since the EIA is known to extend past the dusk terminator, this  
89 current could play a significant role during the night. The third term  $\mathbf{J}_d$  represents the  
90 diamagnetic plasma current which flows in the presence of plasma pressure gradients.  
91 The diamagnetic current in a plasma in equilibrium arises from the balance between the  
92 plasma pressure force and the Lorentz force:

$$93 \quad \nabla P = \mathbf{J} \times \mathbf{B} \quad (4)$$

94 Here,  $P = nk(T_e + T_i)$  is the plasma pressure. Eq. 4 arises from the standard magneto-  
 95 hydrodynamic equations for a plasma when assuming the net plasma flow acceleration is  
 96 0 (steady state), and ignoring gravity [Chen, 2006, eq. 6-1]. We see immediately that  
 97 in equilibrium,  $\mathbf{B} \cdot \nabla P = \mathbf{J} \cdot \nabla P = 0$ . This is an important statement, considering how  
 98 complex the field and plasma distribution geometries may be. Crossing  $\mathbf{B}$  into both sides  
 99 of Eq. 4 and considering current flow perpendicular to  $\mathbf{B}$  results in

$$100 \quad \mathbf{J}_\perp = \frac{\mathbf{B} \times \nabla P}{B^2} \quad (5)$$

101 which is the diamagnetic current  $\mathbf{J}_d$ . It is called diamagnetic because it tends to flow in  
 102 such a way as to diminish the ambient magnetic field. Understanding the diamagnetic  
 103 current and resulting field in the ionosphere is very important for correcting magnetic  
 104 measurements in geomagnetic field modeling [Lühr and Maus, 2010]. The diamagnetic  
 105 current will also be concentrated near the EIA since that is where the plasma pressure  
 106 gradients are greatest. Lühr *et al.* [2003] report magnetic field depletions of up to 5 nT  
 107 at a variety of local times at CHAMP satellite altitude due to these currents. The  $\mathbf{J}_g$  and  
 108  $\mathbf{J}_d$  terms are strictly valid only when the ion collision frequency is small in comparison  
 109 with the gyro-frequency about the magnetic field. Since both the gravity-driven and  
 110 diamagnetic current systems are most prominent in the F-region, where this condition is  
 111 true, these terms are acceptable approximations of their respective currents.

112 The gravity and diamagnetic currents cause secondary electric fields to build up which  
 113 maintain a divergence-free current. These electric fields are contained in the first term  
 114 of Eq. 1. Taking, for example, the gravity-driven current  $\mathbf{J}_g = nm_i \mathbf{g} \times \mathbf{B} / B^2$ , one can  
 115 see that this expression is not necessarily divergence free for an arbitrary  $\mathbf{B}$  and  $n$ , and  
 116 so secondary electric fields will build up to ensure a divergence-free current, which will in

117 turn close the flow of the gravity-driven current. A similar statement can be made for the  
118 diamagnetic term  $\mathbf{J}_d$ . Determining these secondary electric fields and their corresponding  
119 ionospheric currents is discussed in more detail in Sec. 3. In Sec. 4, we discuss our  
120 findings related to the gravity- driven current. In Sec. 5, we present our model of the  
121 diamagnetic currents and their relation to the work of *Lühr et al.* [2003]. Finally we make  
122 some concluding remarks in Sec. 6.

### 3. Modeling the F-region currents with TIEGCM

123 The NCAR TIEGCM (Thermosphere Ionosphere Electrodynamics General Circula-  
124 tion Model) [*Roble et al.*, 1988; *Richmond et al.*, 1992; *Richmond*, 1995] calculates self-  
125 consistently the dynamics, energetics, chemistry and electrodynamics of the ionosphere  
126 and thermosphere. While it would be possible to use the full model to compute the  
127 ionospheric currents, we found it preferable to use only the electrodynamic solver from  
128 TIEGCM, and use external empirical models for the needed ionospheric inputs. The  
129 TIEGCM electrodynamic solver calculates an electric potential  $\Phi$ , and a corresponding  
130 electric field  $\mathbf{E} = -\nabla\Phi$ , which causes  $\mathbf{J}$  in Eq. 1 to satisfy

$$\nabla \cdot \mathbf{J} = 0 \tag{6}$$

131  
132 with suitable boundary conditions.  $\Phi$  is generated by polarization charges which build up  
133 to ensure a divergence-free current. Assuming that the conductivity along geomagnetic  
134 field lines is very high, the electric field component in this direction is negligible, and so  
135 Eq. 6 reduces to a two dimensional equation for the electric potential in magnetic apex  
136 coordinates when integrated along magnetic-field lines from the footpoint at the base of  
137 the ionosphere in the southern hemisphere to the footpoint in the northern hemisphere

138 [Richmond, 1995, eq. 5.23]. The high-latitude boundary condition, providing the cou-  
139 pling between the ionosphere and magnetosphere is provided by the convection model of  
140 Heelis *et al.* [1982]. The equatorial boundary condition is given by the condition that the  
141 meridional field-line-integrated current density must vanish [Richmond, 1995, eq. 5.31].

142 The remaining inputs to the electrodynamic solver are the ionospheric conductivities,  
143 neutral winds, and geomagnetic field. The conductivities rely on the ion, electron and  
144 neutral temperatures and densities. The density and temperature inputs for the electrons  
145 and ions were computed using the International Reference Ionosphere model IRI2007  
146 [Bilitza and Reinisch, 2008]. IRI2007 provides climatologies of electron and ion densities  
147 and temperatures in the altitude range 50km to 2000km. The density and temperature  
148 inputs for the neutral particles were computed using the Mass Spectrometer Incoherent  
149 Scatter model NRLMSISE-00 [Picone *et al.*, 2002]. NRLMSISE-00 models climatological  
150 densities and temperatures of the neutral atmosphere from the Earth's surface to the  
151 exobase. The neutral wind velocity field was computed using the Horizontal Wind Model  
152 HWM07 [Drob *et al.*, 2008; Emmert *et al.*, 2008], which provides the climatologies of the  
153 zonal and meridional wind components. The geomagnetic field input was specified by the  
154 IGRF model.

155 To facilitate the calculation of the ionospheric currents, we developed a subroutine  
156 to calculate the empirical densities, temperatures and winds using the above models,  
157 supply them to the TIEGCM electrodynamic solver, and isolate the gravity-driven and  
158 diamagnetic currents from the output. For the case of the gravity-driven current, this was  
159 accomplished by running the TIEGCM electrodynamic solver twice, once with all current  
160 terms provided, and once with the gravity term set to zero. By subtracting the latter

161 solution from the former, we were able to isolate only the gravity contribution to the total  
162 current, accounting for the secondary electric fields built up. We isolated the diamagnetic  
163 current using the same procedure setting the corresponding term in the current equation  
164 to zero. Although current flows both perpendicular and parallel to  $\mathbf{B}$ , we analyze only  
165 the larger perpendicular component in this study, since the parallel field-aligned currents  
166 are not yet computed by TIEGCM.

#### 4. Features of the gravity-driven current

167 In Figure 1 (top), we plot the total gravity-driven current solution from our simulation  
168 for 0 UT on March 21, 2003 using a solar radio flux index of  $F10.7 = 120$ , displaying  
169 the direction and magnitude of the current at each grid point with arrows. The figure  
170 shows the height-integrated horizontal component of the current perpendicular to  $\mathbf{B}$  from  
171 95km to 640km as a function of geographic latitude and longitude. We see that at low  
172 latitudes, the current is primarily magnetic eastward, following the dip equator. This is  
173 expected from the  $\mathbf{g} \times \mathbf{B}$  term in the current. To illustrate the effect of the secondary  
174 polarization electric fields, we plot in Figure 1 (bottom) the height-integrated current flow  
175  $\mathbf{J}_g$ . In this figure we see the current magnitude diminish significantly during the night,  
176 due to the lower electron density which gives rise to a divergent current. The top figure  
177 does not have this feature, indicating the additional buildup of secondary electric fields  
178 in the pre-dawn local time sector to maintain eastward current flow. One of the most  
179 important open questions regarding the gravity-driven current is the physical mechanism  
180 enabling it to close across this region of low conductivity.

181 In a previous study, *Maus and Lühr* [2006] conjectured that the gravity-driven current  
182 would be restricted by its “bottleneck” of least ion density. Therefore, stronger currents

183 on the day-side would be inhibited by weaker currents on the night-side. Interestingly,  
184 Figure 1 indicates that the night-time current is stronger than one would expect from  
185 the low conductivity. This indicates the build up of strong polarization charges and  
186 induced electric fields to account for this stronger current. To investigate this further, we  
187 analyzed the polarization electric fields as computed by our simulation. We calculated  
188 the polarization electric fields due to the gravity-driven current by again running the  
189 model twice, once with all currents enabled and once with the gravity term turned off,  
190 and taking the difference. Then, the Pedersen and Hall conductivities along with the  
191 polarization electric field components enable the computation of the secondary currents.  
192 We are interested in whether a Pedersen or Hall current can explain the enhanced current  
193 feature seen in the pre-dawn sector. The total gravity driven current can be expressed as

$$194 \quad \mathbf{J}_g^T = \sigma \mathbf{E}_g + \mathbf{J}_g = \sigma \mathbf{E}_g + \frac{nm_i}{B^2} \mathbf{g} \times \mathbf{B} \quad (7)$$

195 where  $\mathbf{E}_g$  is the polarization electric field built up due to the divergent term  $\mathbf{J}_g$ . In  
196 Figure 2, we show the individual contributions from the  $\mathbf{J}_g$  term and the Pedersen and  
197 Hall currents contributing to the  $\sigma \mathbf{E}_g$  term:

$$198 \quad \mathbf{J}_p = \sigma_p \mathbf{E}_g^\perp \quad (8)$$

$$199 \quad \mathbf{J}_h = \sigma_h \hat{b} \times \mathbf{E}_g^\perp \quad (9)$$

200 where  $\sigma_p$  is the Pedersen conductivity,  $\sigma_h$  is the Hall conductivity,  $\mathbf{E}_g^\perp$  is the polarization  
201 electric field component perpendicular to the magnetic field, and  $\hat{b}$  is a unit vector in  
202 the direction of the magnetic field. Figure 2A shows  $\mathbf{J}_g$  in red and the Pedersen current  
203 in blue. Here we see that in the pre-dawn sector where  $\mathbf{J}_g$  is small due to the low  
204 conductivity, the Pedersen current grows substantially to provide current flow across the

205 dawn terminator. We also find in the local time region 1800-2200, the Pedersen current  
206 grows and opposes the flow of  $\mathbf{J}_g$ . Figure 2B shows  $\mathbf{J}_g$  in red and the Hall current in  
207 blue. We see that the Hall current has a localized effect in the pre-dawn sector which  
208 causes current flow across the dawn terminator, and opposes the gravity current flow  
209 during the daytime. The concentrated westward Hall current near the day-time magnetic  
210 equator is the modification of the equatorial electrojet current by the polarization electric  
211 field. Figure 2C shows the sum of the Pedersen and Hall currents in blue against  $\mathbf{J}_g$  in  
212 red. The main conclusion of this figure is that the day-time maximum of the  $\mathbf{J}_g$  current  
213 does not flow uninterrupted into the night, nor does the lower night-time extreme restrict  
214 the current during the day. Instead, an equilibrium current strength is reached between  
215 the two extremes, primarily enabled by the Pedersen current, but also aided by the Hall  
216 current. Built-up polarization charges are physically responsible for the fields driving  
217 these currents.

218 To further explore the structure of this current system, we show in Figure 3 the gravity-  
219 driven current on the same day and UT, holding quasi-dipole latitude fixed at 0 degrees.  
220 The arrows represent the vertical and longitudinal components of the total gravity-driven  
221 current flow  $\mathbf{J}_g^T$ . While we continue to see that the current flow is primarily eastward,  
222 interestingly it becomes stronger at lower altitudes as the night progresses. This is most  
223 likely due to the fact that the current is dominated by  $\mathbf{J}_g$  in the evening, which peaks at  
224 a higher altitude, and by the Pedersen current in the early morning, peaking at a lower  
225 altitude. Looking at this figure along with the latitudinal structure from Figure 1, it  
226 seems probable that there is a divergence of current perpendicular to  $\mathbf{B}$  during the night.  
227 This indicates there could be an additional flow of current along magnetic field lines.

## 5. Features of the diamagnetic current

228 In Figure 4 we plot the diamagnetic current flow calculated from our model at 15 de-  
 229 grees geographic latitude and 17 UT on March 21, 2003, overlaid on top of the electron  
 230 density as provided by IRI. The arrows represent the vertical and longitudinal components  
 231 of the total diamagnetic current flow  $\mathbf{J}_d^T = \sigma \mathbf{E}_d + \mathbf{J}_d$ , where  $\mathbf{E}_d$  is the polarization electric  
 232 field built up due to the divergent term  $\mathbf{J}_d$ . We see here the current flows around the  
 233 density enhancement in a direction which will reduce the ambient geomagnetic field and  
 234 is strongest in regions where the electron density changes most rapidly, as expected. One  
 235 question of great interest is the magnitude of the magnetic field depletion resulting from  
 236 this current. Knowledge of this depletion would aid greatly in correcting satellite mea-  
 237 surements for highly accurate geomagnetic field modeling. Combining Maxwell's equation  
 238  $\nabla \times \mathbf{B} = \mu_0 \mathbf{J}$  with Eq. 4 yields the relation

$$\nabla \left( P + \frac{B^2}{2\mu_0} \right) = \frac{1}{\mu_0} (\mathbf{B} \cdot \nabla) \mathbf{B} \quad (10)$$

240 The left hand side is the sum of plasma pressure and magnetic pressure forces, while the  
 241 right hand side represents magnetic tension due to the curvature of the field lines. By  
 242 defining  $\mathbf{B} = B\hat{b}$ , we can show

$$\frac{1}{\mu_0} (\mathbf{B} \cdot \nabla) \mathbf{B} = \frac{d}{db} \left( \frac{B^2}{2\mu_0} \right) \hat{b} + \frac{B^2}{\mu_0} \frac{1}{R_c} \hat{n} \quad (11)$$

244 where  $b$  is a coordinate which varies along  $\mathbf{B}$ ,  $\hat{b}$  is the unit vector in the direction of  $\mathbf{B}$ ,  $R_c$   
 245 is the radius of curvature of the field line, and  $\hat{n} = R_c \hat{d}\hat{b}/db$  is a vector normal to the field  
 246 line and directed anti-radially. We see that there will be a net tension if the field lines  
 247 are curved or if the magnetic-field strength varies along itself. *Lühr et al.* [2003] proposed  
 248 a solution to Eq. 10 neglecting magnetic tension so the right hand side would vanish,

249 leading to a calculation of the parallel magnetic field perturbation due to the pressure  $P$ :

$$250 \quad b_L = -\frac{\mu_0 P}{B_0} \quad (12)$$

251 Here,  $B_0$  represents the unperturbed ambient field, and the negative sign indicates the  
252 ambient field magnitude is reduced. While Eq. 12 has been used to correct satellite  
253 magnetic measurements for modeling [*Lühr and Maus, 2010*], it remains an open question  
254 as to how accurate the formula is in the presence of curved field lines, as one finds in  
255 the Earth's geomagnetic field. To study this, we directly calculated the magnetic field  
256 resulting from the diamagnetic current computed by our model. This was done by first in-  
257 terpolating the current, represented in magnetic apex coordinates, to geographic spherical  
258 coordinates. The magnetic field of the resulting current was calculated using the toroidal  
259 and poloidal field decompositions of the current vector as described in detail in *Backus*  
260 [1986] and briefly discussed below.

261 A solenoidal vector field  $\mathbf{J}$  may be decomposed as

$$262 \quad \mathbf{J} = \nabla \times \wedge \tilde{p} + \wedge \tilde{q} \quad (13)$$

$$263 \quad \tilde{p}(r, \theta, \phi) = \nabla_1^{-2}(r J_r) \quad (14)$$

$$264 \quad \tilde{q}(r, \theta, \phi) = \nabla_1^{-2}(\wedge \cdot \mathbf{J}_s) \quad (15)$$

265 where  $\wedge = \mathbf{r} \times \nabla$ ,  $\nabla_1 = \nabla - \hat{r} \partial_r$ ,  $\nabla_1^{-2}$  is the inverse of the operator  $\nabla_1^2$ ,  $\mathbf{J}_s = \mathbf{J} - \hat{r} J_r$ ,  
266 and  $\tilde{p}$  and  $\tilde{q}$  are scalar functions representing the poloidal and toroidal components of  $\mathbf{J}$   
267 respectively. It can also be shown that  $\wedge \cdot \mathbf{J}_s = \nabla \cdot (\mathbf{J}_s \times \mathbf{r})$ .

268 Applying the same decomposition to the magnetic field  $\mathbf{B}$  and applying Maxwell's equa-  
 269 tion  $\nabla \times \mathbf{B} = \mu_0 \mathbf{J}$  yields

$$270 \quad \mathbf{B} = \nabla \times \wedge p + \wedge q \quad (16)$$

$$271 \quad q = \mu_0 \tilde{p} \quad (17)$$

$$272 \quad \nabla^2 p = -\mu_0 \tilde{q} \quad (18)$$

273 The advantage of this method is  $\tilde{p}$  and  $\tilde{q}$  can be computed very efficiently using spherical  
 274 harmonic expansions of  $rJ_r$  and  $\wedge \cdot \mathbf{J}_s$  from Eqs. 14-15, since the operator  $\nabla_1^{-2}$  acting  
 275 on a spherical harmonic  $Y_l^m$  simply produces a multiplicative factor of  $-1/l(l+1)$ . The  
 276 toroidal magnetic field coefficients  $q_l^m(r)$  are trivially related to  $\tilde{p}_l^m(r)$  using Eq. 17 and so  
 277 the main task is to solve for the poloidal magnetic field coefficients  $p_l^m(r)$ . Eq. 18 leads to  
 278 a Sturm-Liouville equation for the radial coefficients  $p_l^m(r)$  which can be solved by means  
 279 of Green's functions [*Engels and Olsen, 1998, eq. 9*]:

$$280 \quad p_l^m(r) = \int_a^b G_l(r, s) s^2 \tilde{q}_l^m(s) ds \quad (19)$$

281 where

$$282 \quad G_l(r, s) = \frac{1}{2l+1} \begin{cases} \left(\frac{r}{s}\right)^l \frac{1}{s} & r \leq s \\ \left(\frac{s}{r}\right)^l \frac{1}{r} & r > s \end{cases} \quad (20)$$

283 and the integration is performed radially over the current region, defined by a spherical  
 284 shell  $S(a, b)$  (ie:  $\mathbf{J} = 0$  outside this shell). We solved the integrals in Eq. 19 by reformu-  
 285 lating them in terms of an ordinary differential equation, and then using a Runge-Kutta  
 286 solver. Defining

$$287 \quad y_l^m(r, b) = \int_a^b G_l(r, s) s^2 \tilde{q}_l^m(s) ds \quad (21)$$

288 we can construct an ODE system:

$$289 \frac{d}{ds} y_l^m(r, s) = G_l(r, s) s^2 \tilde{q}_l^m(s) \quad (22)$$

$$290 y_l^m(r, a) = 0 \quad (23)$$

291 where the desired solution is

$$292 p_l^m(r) = y_l^m(r, b) \quad (24)$$

293 Eqs. 22-23 were solved using an adaptive stepsize 8th order Runge-Kutta Prince-Dormand  
294 method. With the  $p_l^m(r)$  and  $q_l^m(r)$  known, Eq. 16 can be used to compute the magnetic  
295 field (see *Engels and Olsen* [1998, eq. 6]). The toroidal/poloidal decomposition method  
296 outlined above for computing magnetic fields is significantly superior to Biot-Savart type  
297 methods, both in terms of efficiency and accuracy, especially in the current region where  
298 Biot-Savart integrals contain a singularity.

299 Once we calculated the magnetic field  $\mathbf{B}_d^T$  from the diamagnetic current  $\mathbf{J}_d^T$ , in order to  
300 compare with Eq. 12, we computed the quantity

$$301 b_c = \mathbf{B}_d^T \cdot \frac{\mathbf{B}_0}{B_0} \quad (25)$$

302 This gives the component of the diamagnetic field in the direction of the ambient field  
303 which is the same quantity calculated by *Lühr et al.* [2003] for the non-tension case.  
304 In Figure 5 we plot  $b_c$  and  $b_L$  as a function of quasi-dipole latitude for three different  
305 local times on March 21, 2003 at an altitude of 350 km. The perturbations are negative,  
306 indicating the effect opposes the ambient geomagnetic field, as expected. We see both  
307 curves exhibit stronger effects near the anomaly density enhancements as expected, but  
308 the prediction of *Lühr et al.* [2003] differs significantly from the computed value at all  
309 latitudes.

310 We are interested in whether this discrepancy is due to an error in the modeling or  
311 in the theoretical prediction. Since the theoretical prediction is strictly valid only when  
312 the ambient field (and the resulting diamagnetic field) have no curvature, we seek a  
313 system in equilibrium in a more complex field geometry with an analytical solution for  
314 comparison. *Krasheninnikov et al.* [1999] provides an explicit solution for the plasma  
315 pressure, diamagnetic current, and total magnetic field for a system in equilibrium in a  
316 dipole field geometry. In such a system, we would start with an ambient dipole field,  
317 supplied for example by a planetary magnetic field or in a laboratory by a small levitated  
318 current ring [*Hasegawa et al.*, 1990]. Plasma is then introduced to the system and the  
319 configuration is allowed to reach a steady state equilibrium. The resulting plasma profile,  
320 plasma current and total magnetic field are restated below and the reader is referred to  
321 *Krasheninnikov et al.* [1999] for more details. The plasma pressure is

$$322 \quad P = P_0 \left( \frac{R_0}{r} \right)^{2\alpha+4} h(x)^{2+4/\alpha} \quad (26)$$

323 where  $P_0$  is the pressure at some reference surface which intersects the dipole equatorial  
324 plane at cylindrical radius  $R_0$ ,  $x = \cos \theta$ ,  $\alpha$  is a constant related to the plasma  $\beta_0 =$  (plasma  
325 pressure) / (magnetic pressure) which is evaluated on the chosen reference surface. To  
326 evaluate the magnetic pressure on this surface, we choose  $B_R$  to be the magnetic field  
327 strength at  $R_0$  on the dipole equatorial plane, so that  $\beta_0 = 2\mu_0 P_0 / B_R^2$ . For plasmas with  
328  $\beta_0 \ll 1$ ,  $\alpha = 1 - 512\beta_0/1001$ . Finally,  $h(x)$  is a function which satisfies the nonlinear  
329 dipole Grad-Shafranov equation and in the small  $\beta_0$  limit is given by

$$330 \quad \frac{h(x)}{1-x^2} = 1 - \frac{192}{1001} \beta_0 \sum_{i=1}^5 c_i [1 - (1-x^2)^i] \quad (27)$$

331 with the coefficients  $c_i = (1, \frac{5}{12}, \frac{35}{144}, \frac{21}{128}, \frac{77}{640})$  [Krasheninnikov et al., 1999, eqs. 12,15]. The

332 diamagnetic current and total magnetic field are then given by

$$333 \quad \mathbf{J} = \frac{\beta_0(2 + \alpha)B_R R_0^{\alpha+2} \sin \theta}{\mu_0 r^{\alpha+3}} h(x)^{1+4/\alpha} \hat{\phi} \quad (28)$$

$$334 \quad \mathbf{B} = \frac{B_R R_0^{\alpha+2}}{\alpha r^{\alpha+2}} \left[ \hat{\theta} \frac{\alpha h}{\sin \theta} - \hat{r} \frac{dh}{dx} \right] \quad (29)$$

335 It can be verified that the MHD equilibrium equations and Maxwell's equations are sat-  
 336 isfied by this field and plasma configuration. We see that in the vacuum limit,  $\beta_0 \rightarrow 0$ ,  
 337  $\alpha \rightarrow 1$ ,  $\mathbf{J} \rightarrow 0$ ,  $h \rightarrow \sin^2 \theta$  and  $\mathbf{B}$  reduces to a simple dipole field. This field can be  
 338 expressed as

$$339 \quad \mathbf{B}_v = \frac{F}{2\pi} \frac{R_0}{r^3} \left[ \sin \theta \hat{\theta} + 2 \cos \theta \hat{r} \right], \quad (30)$$

340 where  $F = 2\pi R_0^2 (B_R/\alpha)$  is the magnetic flux through the dipole equatorial plane for  
 341  $r > R_0$ . If we consider  $R_0$  to be representative of the mean height of the ionosphere, it is  
 342 more physically realistic to hold the flux  $F$  constant than  $B_R$  when analyzing the vacuum  
 343 limit, because the field strength in the equatorial ionosphere is not constant when plasma  
 344 pressure changes, but the displacement of magnetic flux out of the ionosphere by plasma  
 345 pressure does tend to reduce the ionospheric field and increase the field at high altitudes  
 346 in a manner analogous to the model of Krasheninnikov et al. [1999]. The analytical field  
 347 depletion due to the diamagnetic current can now be defined as

$$348 \quad b_A = |\mathbf{B}| - |\mathbf{B}_v| \quad (31)$$

349 This can be directly compared with Eq. 12, where  $B_0 = |\mathbf{B}_v|$ . In Figure 6 we plot  
 350 the analytic result  $b_A$  against the theoretical prediction  $b_L$  as a function of  $r/R_0$  for our  
 351 test case for four different latitudes with the following parameters:  $\beta_0 = 0.01$ ,  $F =$   
 352  $1.2 \times 10^{10} \text{Wb}$ ,  $R_0 = R_E = 6371.2 \text{km}$ . We also plot the magnitude of the tension force (the

353 RHS of Eq. 10) on the second vertical axis. We see that in the equatorial region, where  
354 the tension magnitude is smallest,  $b_L$  has the best agreement with  $b_A$ . The agreement in  
355 the  $30^\circ$  and  $45^\circ$  latitude plots is significantly worse, since the magnetic tension is higher.  
356 In these plots, the  $b_L$  prediction of *Lühr et al.* [2003] is small in magnitude, primarily due  
357 to the plasma pressure  $P$  dropping off very rapidly at high latitudes. To further illustrate  
358 the effect, we plot in Figure 7 the analytic result  $b_A$  against the theoretical prediction  
359  $b_L$  as a function of latitude, holding  $r$  fixed at  $R_0$ . Magnetic tension is again plotted on  
360 the second vertical axis. We find good agreement at low latitudes where the tension is  
361 minimum, and significant disagreement at mid and high latitudes where tension is large.  
362 Since the Earth's geomagnetic field has a large dipole moment, it is likely that magnetic  
363 tension plays a significant role in the ionospheric diamagnetic effect and cannot be ignored.

## 6. Conclusion

364 We have successfully modeled the F-region gravity-driven and diamagnetic current sys-  
365 tems using the NCAR TIEGCM model with empirical density, wind and temperature  
366 inputs. The global gravity-driven current structure exhibits a strong eastward flow at low  
367 latitudes primarily following the equatorial ionization anomaly as expected. The current  
368 strength during the night is significantly higher than expected from the low conductiv-  
369 ity, but not as high as the strongest local daytime current magnitude as computed from  
370  $\mathbf{J}_g$ . This is due to the buildup of significant polarization electric fields in the pre-dawn  
371 sector as well as during the day. During the night, the gravity-driven current strength  
372 descends in altitude and diverges perpendicular to  $\mathbf{B}$ , implying that there is also a sig-  
373 nificant field-aligned current, which is not currently calculated. The diamagnetic current  
374 structure has also been presented, which is also prominent near the EIA. The magnitude

375 of its ambient field depletion has been calculated by directly computing its magnetic field.  
376 These field depletions were compared with the theoretical prediction of *Lühr et al.* [2003]  
377 with significant discrepancies. These discrepancies could be due to magnetic tension of  
378 the curved geomagnetic field, which was not accounted for by the theoretical prediction.  
379 They could also be due to inaccuracies in the TIEGCM modeling, such as the neglect of  
380 the influence of parallel currents, which we plan to investigate in a future study. With  
381 this modeling framework in place, the next step will be to compare satellite data with  
382 our modeling predictions to determine the model's accuracy. The benefits of having an  
383 accurate ionospheric current model include creating more accurate ionospheric magnetic  
384 field models, as well as gaining the ability to further analyze high-accuracy magnetic field  
385 measurements from future satellite missions.

## Acknowledgments

386 This work was supported in part by NASA grant NNX08AG09G. The National Center  
387 for Atmospheric Research is sponsored by the National Science Foundation. We would  
388 also like to thank Wenbin Wang for helpful comments on an earlier draft.

## References

- 389 Backus, G. (1986), Poloidal and toroidal fields in geomagnetic field modeling, *Rev. Geo-*  
390 *phys.*, *24*(1), 75–109.
- 391 Bilitza, D., and B. W. Reinisch (2008), International Reference Ionosphere 2007:  
392 improvements and new parameters, *J. Adv. in Space Res.*, *42*(4), 599–609, doi:  
393 10.1016/j.asr.2007.07.048.

394 Chen, F. F. (2006), *Introduction to plasma physics and controlled fusion. Volume 1:*  
395 *Plasma physics, 2nd edition*, Springer, New York.

396 Drob, D. P., et al. (2008), An empirical model of the earth's horizontal wind fields:  
397 HWM07, *J. Geophys. Res.*, *113*, A12304, doi:10.1029/2008JA013668.

398 Eccles, J. V. (2004), The effect of gravity and pressure in the electrodynamics of the  
399 low-latitude ionosphere, *J. Geophys. Res.*, *109*, A05304, doi:10.1029/2003JA010023.

400 Emmert, J. T., D. P. Drob, G. G. Shepherd, G. Hernandez, M. J. Jarvis, J. W. Meri-  
401 wether, R. J. Niciejewski, D. P. Sipler, and C. A. Tepley (2008), Dwm07 global empirical  
402 model of upper thermospheric storm-induced disturbance winds, *J. Geophys. Res.*, *113*,  
403 A11319, doi:10.1029/2008JA013541.

404 Engels, U., and N. Olsen (1998), Computation of magnetic fields within source regions of  
405 ionospheric and magnetospheric currents, *J. Atmos. Sol. Terr. Phys.*, *60*, 1585–1592.

406 Forbes, J. M. (1981), The equatorial electrojet, *Reviews of Geophysics and Space Physics*,  
407 *19*(3), 469–504.

408 Hasegawa, A., L. Chen, and M. Mauel (1990), A d-3he fusion reactor based on a dipole  
409 magnetic field, *Nucl. Fusion*, *30*, 2405.

410 Heelis, R., J. Lowell, and R. Spiro (1982), A model of the highlatitude ionospheric con-  
411 vection pattern, *J. Geophys. Res.*, *87*, 6339–6345.

412 Krasheninnikov, S. I., P. J. Catto, and R. D. Hazeltine (1999), Magnetic dipole equilibrium  
413 solution at finite plasma pressure, *Phys. Rev. Lett.*, *82*(13).

414 Lühr, H., and S. Maus (2006), Direction observation of the F region dynamo cur-  
415 rents and the spatial structure of the EEJ by CHAMP, *Geophys. Res. Lett.*, *33*, doi:  
416 10.1029/2006GL028374.

417 Lühr, H., and S. Maus (2010), Solar cycle dependence of quiet-time magnetospheric cur-  
418 rents and a model of their near-Earth magnetic fields, *Earth Planets Space*, *62*, 843–848.

419 Lühr, H., M. Rother, S. Maus, W. Mai, and D. Cooke (2003), The diamagnetic effect of  
420 the equatorial Appleton anomaly: Its characteristics and impact on geomagnetic field  
421 modeling, *Geophys. Res. Lett.*, *30*(17), doi:10.1029/2003GL017407.

422 Maeda, H., T. Iyemori, T. Araki, and T. Kamei (1982), New evidence of a meridional  
423 current system in the equatorial ionosphere, *Geophys. Res. Lett.*, *9*, 337–340.

424 Maus, S., and H. Lühr (2006), A gravity-driven electric current in the Earth’s ionosphere  
425 identified in CHAMP satellite magnetic measurements, *Geophys. Res. Lett.*, *33*, L02812,  
426 doi:10.1029/2005GL024436.

427 Maus, S., C. Manoj, J. Rauberg, I. Michaelis, and H. Lühr (2010), NOAA/NGDC candi-  
428 date models for the 11th generation International Geomagnetic Reference Field and the  
429 concurrent release of the 6th generation Pomme magnetic model, *Earth Planets Space*,  
430 *62*, 729–735.

431 Picone, J. M., A. E. Hedin, D. P. Drob, and A. C. Aikin (2002), NRLMSISE-00 empirical  
432 model of the atmosphere: statistical comparisons and scientific issues, *J. Geophys. Res.*,  
433 *107*, doi:10.1029/2002JA009430.

434 Richmond, A. D. (1995), Ionospheric electrodynamics using magnetic apex coordinates,  
435 *J. Geomag. Geoelec.*, *47*, 191–212.

436 Richmond, A. D., E. C. Ridley, and R. G. Roble (1992), A thermosphere/ionosphere  
437 general circulation model with coupled electrodynamics, *Geophys. Res. Lett.*, *6*, 601–  
438 604.

439 Rishbeth, H. (1971), The F-layer dynamo, *Planet. Space Sci.*, *19*, 263–267.

440 Roble, R. G., E. C. Ridley, A. D. Richmond, and R. E. Dickinson (1988), A coupled  
441 thermosphere/ionosphere general circulation model, *Geophys. Res. Lett.*, *15*, 1325–1328.

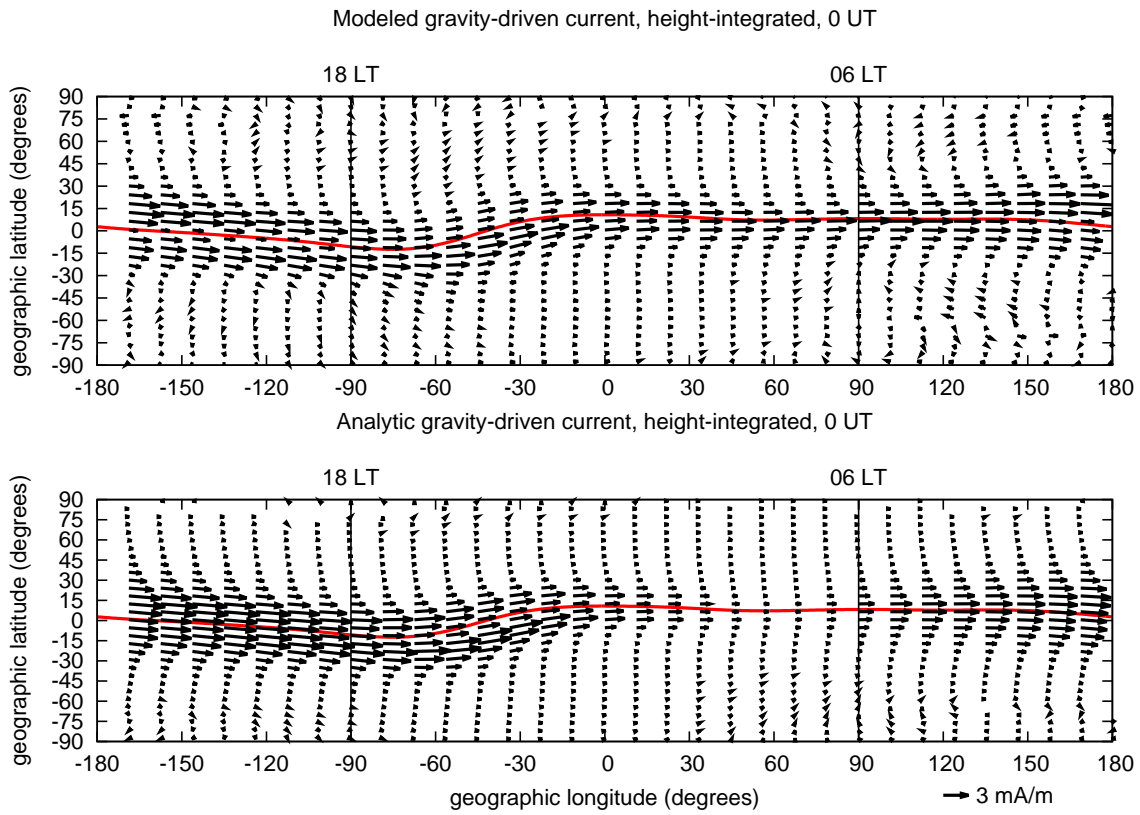


**Figure 1.** Height-integrated gravity driven currents for (top) model calculation and (bottom) analytic term  $\mathbf{J}_g$  for 0 UT on March 21, 2003. Vertical lines indicate the position of 0600 and 1800 local times. Red curve indicates position of the magnetic equator at 350km altitude.

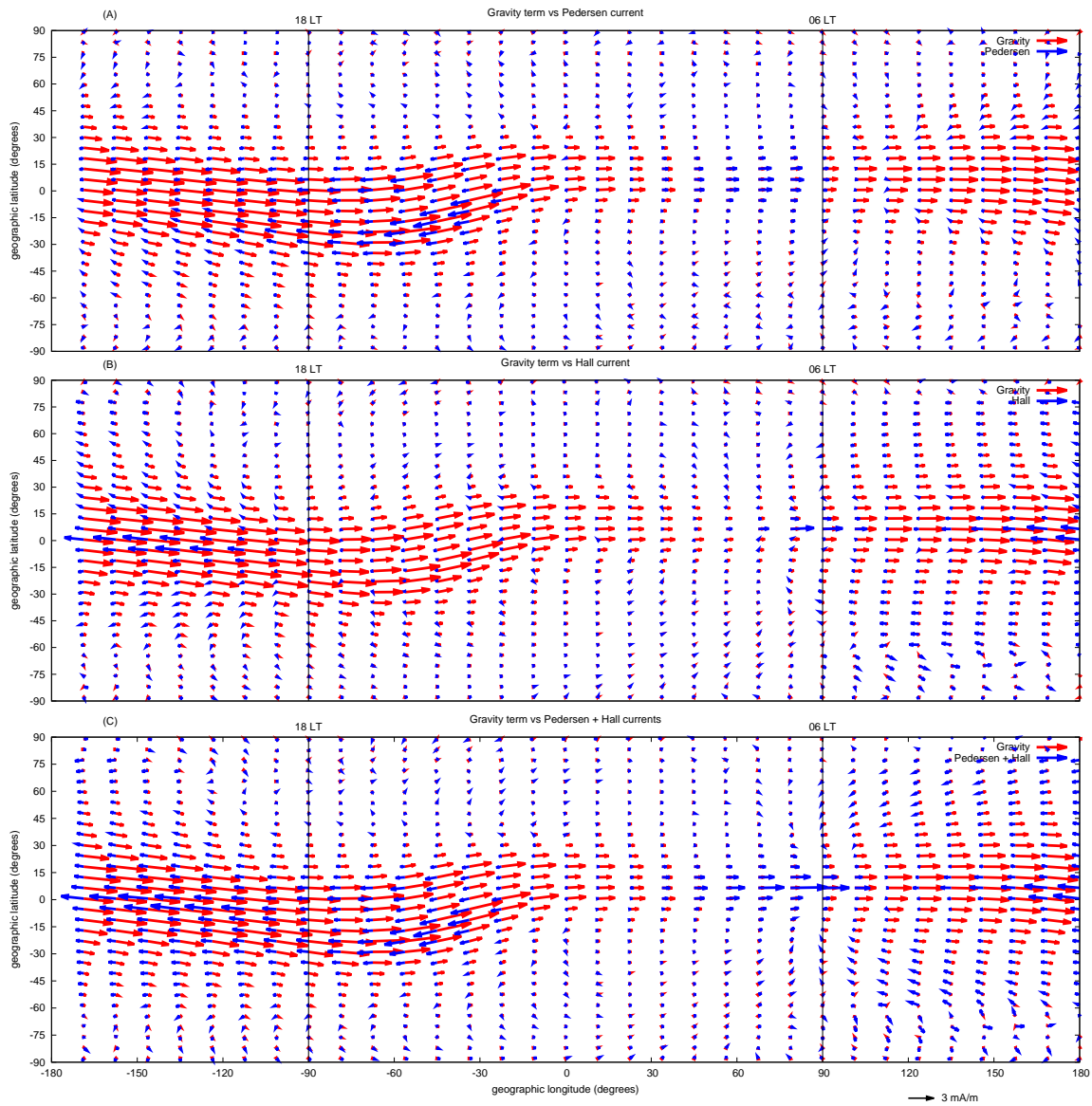


**Figure 2.** (A)  $\mathbf{J}_g$  term (red) with Pedersen current derived from polarization electric field (blue). (B)  $\mathbf{J}_g$  term (red) with Hall current derived from polarization electric field (blue). (C)  $\mathbf{J}_g$  term (red) with sum of Pedersen and Hall currents derived from polarization electric field (blue). All figures represent height-integrated currents at 0 UT on March 21, 2003.

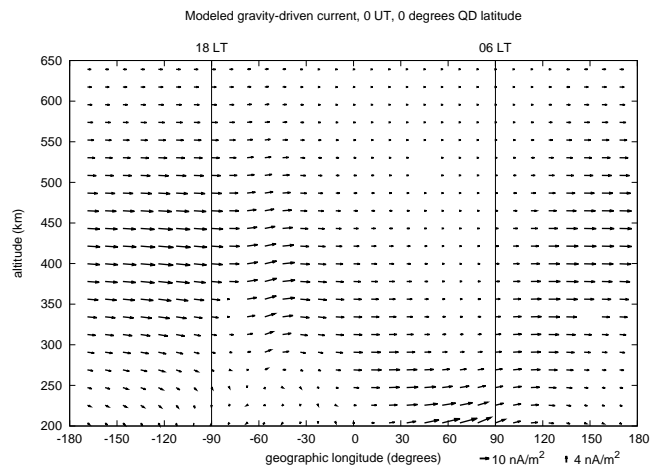


**Figure 3.** Gravity driven current as a function of longitude and altitude for 0 UT on March 21, 2003. Quasi-dipole latitude is held fixed at 0 degrees. Vertical lines indicate the positions of 0600 and 1800 local times. Due to the much larger distance covered by the horizontal axis, two separate scaling factors were used in the vertical and horizontal directions as shown, in order to better visualize the current flow.

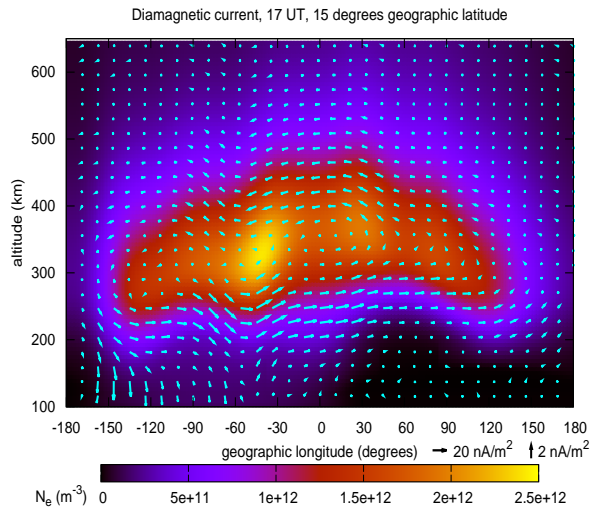


**Figure 4.** Diamagnetic current flow along with electron densities as a function of longitude and altitude for 17 UT and 15 degrees geographic latitude on March 21, 2003. Due to the much larger distance covered by the horizontal axis, two separate scaling factors were used in the vertical and horizontal directions as shown, in order to better visualize the current flow.

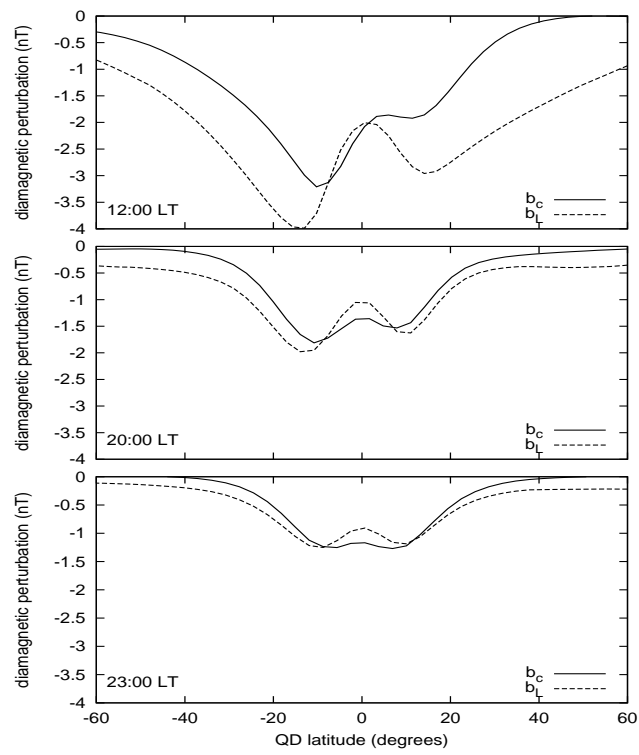


**Figure 5.** Calculated diamagnetic field (solid) perturbation with theoretical prediction (dashed) as a function of quasi-dipole latitude for 17 UT on March 21, 2003, altitude 350 km for 3 different local times.

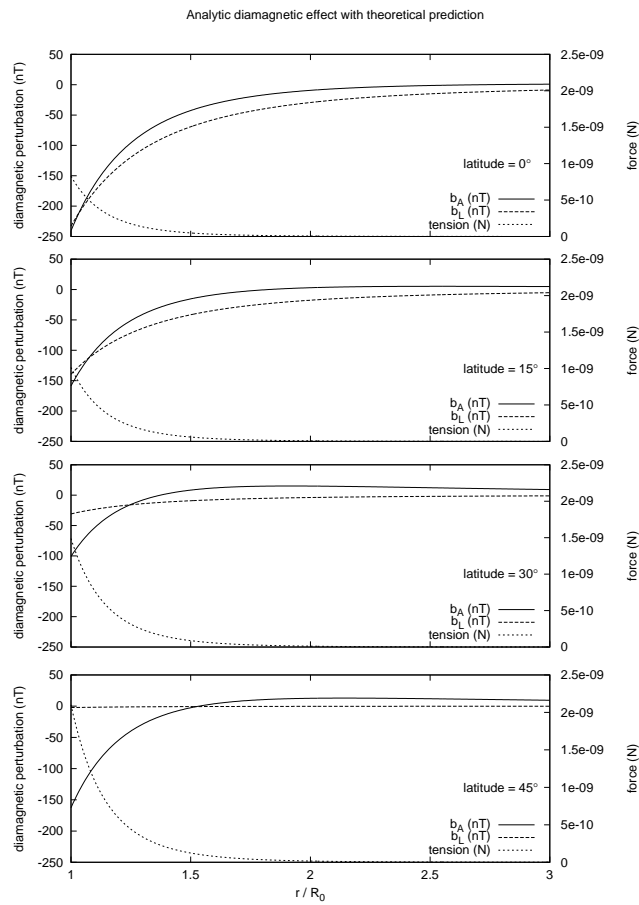


**Figure 6.** Analytic diamagnetic field perturbation ( $b_A$ , solid) with theoretical prediction ( $b_L$ , dashed) for dipole equilibrium test case, plotted as a function of  $r/R_0$  for four different latitudes. Tension force magnitude (dotted) plotted on second vertical axis.

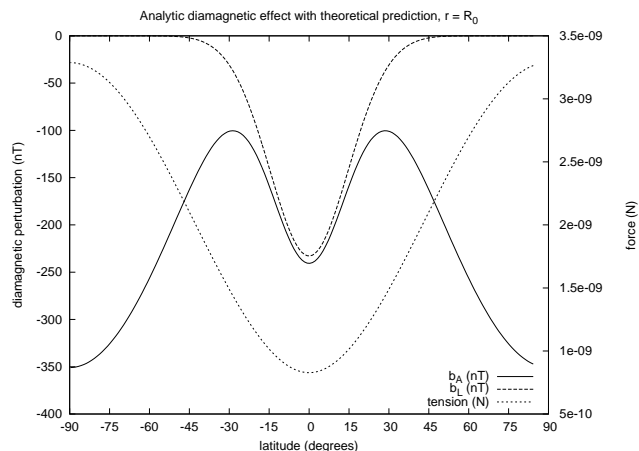


**Figure 7.** Analytic diamagnetic field perturbation ( $b_A$ , solid) with theoretical prediction ( $b_L$ , dashed) for dipole equilibrium test case, plotted as a function of latitude for  $r = R_0$ . Tension force magnitude (dotted) plotted on second vertical axis.